Title
Correlating the phase evolution and anionic redox in Co-Free Ni-Rich layered oxide cathodes

Authors
Li, Ning
Sallis, Shawn
Papp, Joseph K
et al.

Publication Date
2020-12-01

DOI
10.1016/j.nanoen.2020.105365

Peer reviewed

Correlating the Phase Evolution and Anionic Redox in Co-Free Ni-Rich Layered Oxide Cathodes

Ning Li,[a] Shawn Sallis,[b] Joseph K. Papp,[c] Bryan D. McCloskey,[a,c] Wanli Yang,[b,*] Wei Tong[a,*]

[a] *Energy Storage and Distributed Resources Division, Lawrence Berkeley National Laboratory, Berkeley, CA 94720 USA*

[b] *Advanced Light Source, Lawrence Berkeley National Laboratory Berkeley, Berkeley, CA 94720, USA*

[c] *Department of Chemical and Biomolecular Engineering, University of California, Berkeley, CA 94720 USA*

** Correspondence: Wei Tong (weitong@lbl.gov), Wanli Yang (wlyang@lbl.gov)*

Abstract

Current trend of high-capacity Ni-rich layered cathode is to develop high-Ni and low-Co or Co-free oxides. The high Ni content layered oxides provide great advantages in capacity, cost and environmental benignity, similar to $LiNiO_2$ parent compound. But they also inherit drawbacks in structural and chemical instability at high voltages upon cycling. Elemental substitution plays a profound role in addressing these challenges. This work elucidates the roles of Al doping in cationic redox and anionic oxygen activity in $LiAl_xNi_{1-x}O_2$ using combined X-ray absorption spectroscopy (XAS), resonant inelastic X-ray scattering (RIXS) as well as *operando* differential electrochemical mass spectrometry (DEMS). Using synchrotron wide-angle X-ray scattering (WAXS), we extrapolate a general principle of phase transition and its coupling with lattice anionic oxygen redox. These findings shed light on the advancement of high-capacity, stable-cycling and safe-operating Ni-rich cathode materials for next generation Li-ion batteries.

Keywords

Li-ion battery cathode, Al doped Ni-rich layered oxide, anionic oxygen redox, oxygen release, phase transition

1. Introduction

Nowadays, Ni-rich layered oxides have been considered as the best Li-ion battery cathode choice in the near term to meet the ever increasing energy requirement for the large-scale applications such as electric vehicles (EVs).[1-3] Development of Ni-rich layered cathode can be traced back to parent $LiNiO_2$, in pursuit of even lower-cost and less-toxic material alternative to $LiCoO_2$,[4-8] to the most recent derivatives of $LiNi_{1-x-y}Co_xAl_yO_2$ (NCA) and $LiNi_{1-x-y}Mn_xCo_yO_2$ (NMC) for high capacity and long cycling.[9-15] Layered $LiNO_2$ suffers from various challenges in synthesis of stoichiometric materials, bulk phase transition, surface stability and thermal stability upon exposure to electrolytic solution at high voltages.[16-25] Today's NCA cathode has demonstrated certain success for the practical use in EVs, however, they are still being challenged by the ever increasing needs of higher energy and longer life for the mass adoption of EVs. The dilemma between high energy delivery and long cycle life for Ni-based layered oxide is essentially related to the anisotropic volume change of the electrode material, originating from the multiple phase transition during the charge-discharge process.[26-28]

Recently, a clear trend of increasing Ni content to 0.9 or even higher has been witnessed for the implementation of high-capacity cathodes of low Co or no Co.[29-32] Such layered electrodes with high Ni content appear to share common properties to $LiNiO_2$, mostly from structural and thermal points of view upon delithiation.[33-37] In NCA or optimized NMC cathodes, the role of Co in preventing Li/Ni intermixing and maintaining good layered structure has been quite well understood based on the early research of the binary Ni-Co system. Other beneficial dopants at a marginal content are Al, Mg and Ti etc.[29, 30, 38], which are claimed to alleviate the detrimental H2 to H3 phase transition to some extent.[29, 39, 40] An abundance of research on these compounds was directed towards the performance target within a relatively low voltage limit of <4.3 V for the safe operation of carbonate electrolytes.

Currently, high capacity demand urges the battery operation to higher voltages (>4.3 V), where participation of lattice oxygen is seriously concerned, especially after oxygen activity has been

experimentally verified in various layered oxide cathodes.[41-45] Note lattice oxygen activity here includes both irreversible oxygen loss and reversible oxygen redox.[46-53] Gas release from the active cathodes at high voltages is well known and often believed to be coupled with electrolyte decomposition. The explicit contribution of lattice oxygen in gas generation remains elusive. Similarly, research on the contribution of lattice oxygen redox to charge compensation in these materials is sparse compared to that of transition metal at high voltages. As such, no correlation between transition metal/metal and oxygen activity at high voltages has been established yet, which requires a comprehensive study of cationic and anionic redox behaviors at highly charged states.[54-57]

Indeed, theoretical calculations predicted the possible charge transfer from lattice oxygen in conventional layered oxides even earlier than those reports in Li-rich layered cathode, although little direct experimental evidence was available at that time.[55, 58-62] Since then, oxygen redox contribution in conventional layered cathode has been staggering with the excitement of continuous optimization of NMC electrode. Until recently, participation of anionic lattice oxygen redox at high Li^+ (de)intercalation of layered $LiCoO_2$ was experimentally verified.[63] The rising trend in implementing high-capacity Ni-rich layered oxide at high voltages triggers renewed interests and a definitive need to study the oxygen activity in these promising cathodes. It is of significant importance to understand the role of substituting element on oxygen activities including both irreversible oxygen loss and reversible lattice oxygen redox, which will enable us to reconsider the choice of substituting element for high voltage operation.

In this work, the role of Al substitution in $LiNiO_2$ is investigated in a relatively wide range (0.05 - 0.2) and a large array of material properties such as structure, electrochemistry, electrode kinetics, charge compensation of cationic Ni and anionic O as well as irreversible oxygen release. Al is obviously an important dopant in Ni-rich layered oxide cathodes, e.g., the well-known NCA, which has been recently revisited to explore the possibility to achieve an even higher practical capacity at high voltages. The increasing demand of energy also poses a safety concern, and Al was originally introduced to

improve the thermal stability. So there is a necessity to examine the effect of higher Al content, especially at highly charged state.[64] Additionally, Al is present as 3+, so substituting Ni by Al does not change the stoichiometry or Ni valence state. Furthermore, Al is electrochemically inactive, introducing Al naturally decreases the accessible cationic Ni redox, which warrants enough Li^+ for the oxygen redox, if any. Comprehensive understanding of the correlation between Al substitution and oxygen at high voltages will shed light on further development of technologically important Ni-rich layered oxide cathode for high-capacity and long-term cycling.

2. Materials and Methods

2.1. Material synthesis and characterization

$LiAl_xNi_{1-x}O_2$ samples were prepared by high-energy milling $Ni(OH)_2$, $Al(OH)_3$ and Li_2CO_3 (Sigma Aldrich) for 3 h, followed by high temperature calcination in oxygen atmosphere at 750 ºC for 15 h. Scanning electron microscopy (SEM) was conducted on a JEOL JSM-7000F equipped with a Thermo Scientific EDS detector. Powder X-ray diffraction (XRD) patterns were collected on a Bruker D2-Phaser with Cu Kα radiation (λ = 1.54178 Å). XRD patterns were further analyzed by conventional Rietveld method using the general structure analysis system package with the graphical user interface (EXPGUI).

Ex situ synchrotron X-ray scattering was performed on beamline endstation 11-3 equipped with a bent flat, side-scattering Si (311) monochromator at a fixed energy of 12,700 eV (λ = 0.9765 Å) at Stanford Synchrotron Radiation Light source (SSRL). Hard X-ray absorption spectroscopy (XAS) was performed on beamline endstation 2-2 in a transmission mode using a (220) monochromator at SSRL. Energy was calibrated by the spectrum of Ni metal foil reference. X-ray absorption near-edge spectroscopy (XANES) data were analyzed using SIXPACK software. Soft XAS measurements were carried out on beamline endstation 10-1 at SSRL. The Ni *L*-edge and O *K*-edge spectra were acquired

under ultrahigh vacuum (10-9 Torr) in a single load at room temperature using total electron yield (TEY) *via* the drain current.

2.2. Characterization of oxygen chemical state

RIXS maps were collected in high-efficiency iRIXS endstation at Beamline endstation 8.0.1 at the Advanced Light Sources (ALS). Sample surface was mounted 45º to the incident beam, and the outgoing photon direction along the RIXS spectrograph is 90º. RIXS resolving power and other technical details could be found in our previous report.[52, 53] *Operando* DEMS was conducted on a customized Swagelok type cell connected to a high-pressure gas chromatography valve. The details were described in previous publications.[52, 65] DEMS cell was initially rested at the open circuit voltage for 6 h and charge/discharge was done under potentiostatic control using a Bio-Logic SP-300 potentiostat.

2.3. Electrochemical characterization

Electrode slurry was prepared by mixing 80 wt% of active material, 10 wt% of polyvinylidene fluoride (PVdF) binder and 10 wt% acetylene carbon black (Denka, 50% compressed) in N-methylpyrrolidone (NMP). The slurry was casted on carbon-coated aluminum current collectors (Exopack Advanced Coatings) using a doctor blade set to 150 μm height. The slurry was then dried under vacuum at 120 ºC overnight and dried film was punched to get disk electrodes with a diameter of ½ inch. Typical loading of the active material is 2.5 – 3.0 mg cm^{-2}. 2032-type coin cells, consisting of the as-produced active materials, Li metal anode, Celgard 2400 separator, were assembled in an Ar-filled glovebox (O_2, H_2O < 0.1 ppm). 1M $LiPF_6$ dissolved in 1:2 w/w ethylene carbonate - diethyl carbonate (Daikin) was used as the electrolyte. Galvanostatic charge and discharge and galvanostatic intermittent titration technique (GITT) measurements were performed at designated voltage ranges on a Maccor 4200 battery cycler. 1C capacity was defined as 200 mAh g^{-1}. All the cycled electrodes were immediately disassembled and collected from the cells and washed by DMC solvent multiple times to ensure the removal of soluble surface species. All the dried electrodes were transferred into the experimental

vacuum chamber through a specially designed sample transfer kit in an Ar-filled glove box to avoid any air exposure.

3. Results and Discussion

3.1. Characterization of Al-doped layered oxides

Al doped $LiNiO_2$ materials are synthesized by solid-state calcination of high-energy milled precursor mixtures of $Ni(OH)_2$, $Al(OH)_3$ and Li_2CO_3. Al doping content is 0, 0.05, 0.10 and 0.20, and the resultant materials are denoted as LNO, LANO-05, LANO-10 and LANO-20, respectively. The as-produced samples are composed of agglomerated secondary particles with submicron-size primary particles (**Figure S1**) with homogeneous elemental distribution of Al, Ni and O (**Figure S2-4**). Material structures of Al-doped samples are investigated by X-ray diffraction (XRD) combined with Rietveld refinement (**Figure 1**). All XRD patterns can be well indexed by layered α-$NaFeO_2$ structure with $R\bar{3}m$ symmetry. Additional diffraction peaks around 24 and 33º are observed in the LANO-20 sample, which is related to Li_4AlO_5 (~2.0 wt%), suggesting Al content is reaching the solid solution limit under the current synthesis condition.[66] The well-split (006)/(012) and (108)/(110) peaks, around 37.5 and 64.8º, respectively, in all patterns indicate the good crystallization in all samples. Rietveld refinement results (**Figure 1a-d**) reveal a good consistency between calculated and experimental patterns, but a continuous change of lattice parameter *a* and *c* with increasing Al content (**Figure 1e**), suggesting Al is successfully doped in the crystal lattice of the final products. It is worth noting that the *a* value decreases and *c* value increases with increasing Al amount, which is consistent with previous report.[67] Furthermore, *c*/*a* ratio, an indicator of layered structure, increases with Al content, but Li/Ni intermixing gradually increases as well (**Figure 1f**). Impact of Al doping on material structural is multi-faceted: the preference of Al^{3+} in the 3b Ni site due to their similar ionic radii (Al^{3+}: 0.53 Å and Ni^{3+}: 0.56 Å) promotes the presence of Ni in Li layer, therefore, higher Li/Ni intermixing; meanwhile, the presence of Ni in the Li layer can act as

pillars to stabilize the layered structure, although the excess Li/Ni intermixing likely blocks the Li^+ diffusion.

3.2. Electrochemical performance and electrode kinetics

Electrochemical performance of Al doped samples is evaluated in a wide voltage window to probe the possible oxygen activity. First, they are electrochemically evaluated at various charge cutoff voltages to understand the effect of Al substitution on the charge and discharge capacity at different charge voltages (**Figure 2**). Charge cutoff voltage is selected between 4.3 and 5.0 V with same discharge voltage of 2.7 V (**Figure 2a-c**). LANO-05 sample displays a gradually increase in reversible capacity from 182, 196, 203 to 207 mAh g^{-1} at 4.3, 4.5, 4.8 and 5.0 V, respectively. For LANO-10 sample, the corresponding discharge capacity is 149, 179, 197 and 200 mAh g^{-1}, in comparison to 140, 146, 182 and 186 mAh g^{-1} for LANO-20 sample. Clearly, all samples exhibit higher reversible capacities with increasing charge cutoff voltage, but only marginal capacity gain from 4.8 to 5.0 V. In contrast, more discharge capacity gain is revealed in LANO-10 (32.2%) and LANO-20 (30%) samples compared to LNAO-05 (11.5%) from 4.3 to 4.8 V charge cutoff, although the overall discharge capacity decreases with the incorporation of more inactive Al (decreased available Ni redox). It is noted that a lower coulombic efficiency is obtained in LANO samples at high charge cutoff voltages. The charge capacity is not affected when charged to high voltages (i.e., 5 V), where oxygen oxidation takes place to compensate for the additional Li^+ extraction. However, the oxidized oxygen is reactive and results in oxygen and CO_2 outgassing upon exposure to electrolyte, which definitely contributes to the high irreversible capacity.

Additionally, the voltage profiles in the high voltage region change upon Al substitution, which should be related to the phase transition, i.e., H2-H3 phase transition, in Ni-rich layered cathode.[26-28] Evidence of the structural evolution upon (de)lithiation can be revealed from the dQ/dV plots (**Figure 2d-f**). LANO-05 sample largely inherits multiple phase transition from LNO, as evidenced by multiple

pairs of redox peaks (**Figure S5**). While for LANO-10 and LANO-20 samples, the redox peaks become less sharp and pronounced, indicating the great suppression of multiple phase transition with Al doping. The first pair of redox peaks above 4.0 V, corresponding to unfavorable H2-H3 transition, shift to higher voltages with increasing Al content, further confirming Al doping mitigates the phase transition.

We further evaluate the electrode kinetics for all three samples by galvanostatic intermittent titration technique (GITT), illustrating the polarization at different states of charge (**Figure 2g-i**). In comparison, LANO-05 and LANO-10 samples exhibit relatively low polarization below 4.5 V, indicating improved electrode kinetics. While above 4.5 V charge, a high polarization observed for all samples is possibly due to the parasitic reactions such as electrolyte decomposition, gas evolution etc., which will be discussed in more detail later. LANO-20 sample displays an even higher polarization during charge and discharge, which may result from the high Li^+ diffusion barrier originating from Li/Ni intermixing. Meanwhile, when comparing the GITT curves at 4.8 and 5.0 V charge cutoff, a polarization increase during discharge is revealed for all samples, suggesting the unfavorable reactions at exceptionally high voltages, while the higher polarization during discharge of LANO-20 suggests the side reaction is more severe in this sample.

3.3. Phase transition and crystal lattice collapse

In line with the phase evolution revealed by differential capacity, *ex situ* wide-angle X-ray scattering (WAXS) was performed at various charged states (**Figure 3**). For the pristine LNO sample, (003) peak located at 11.70º is present as H1 phase (O3), and then gradually shifts to lower diffraction angle, reaches the lowest 2θ value of 11.64º to form H2 phase. At 4.3 V, (003) peak splits to two peaks due to phase transition from H2 to H3, and finally evolves to one major peak related to H3 phase at 12.60º at the end of charge. This large shift from H2 to H3 phase can result in shortened interlayer spacing. With Al doping, all samples show similar peak shift, however, to much less extent, i.e., (003) peak shifts

to a lower 2θ value at the end of charge, while the other major peaks display a similar anisotropic change by shifting continuously to a higher 2θ value during charge.[16, 17, 68]

To better visualize the impact of Al doping on the phase transition, lattice parameter *c* is calculated to investigate its change during charge and discharge for all samples (**Figure 4**). **Figure 4a** shows lattice parameter *c* collapses at different charge voltage for each sample, 4.3 V for LNO and LANO-05, 4.5 V for LANO-10 and 4.8 V for LANO-20, which slightly increases with Al content. In sharp contrast, lattice parameter *c* perhaps follows a general collapse trend and shows strong correlation with Li^+ content, but not charge voltage. It can be seen that lattice *c* value can be well fitted with a common curve for all samples and *c* lattice collapses at ~70% Li^+ extraction (**Figure 4b**). More importantly, the degree of lattice *c* collapse is obviously different for all samples, and Al doping is effective to mitigate *c* collapse as well as the interlayer spacing of crystal lattice (**Figure 4c, d**). Meanwhile, the total extractable Li^+ content during cycling does not show a great difference for all samples, despite the varied available Ni redox, inferring the possibly greater involvement of oxygen activity. Furthermore, the collapse of lattice *c* is only Li^+ content dependent rather than voltage or Ni content (or redox), which remains consistent with NMC and NCA systems.[68] This phenomenon brings one's attention to reconsider the possible reasons, as the collapse of *c* inevitably results in the shortening of O-O bond between interlayers, so the *c* collapse process maybe coupled with the participation of bulk lattice oxygen redox, which will be discussed later.[69, 70]

3.4. Charge compensation of bulk cationic and anionic redox

To investigate the charge compensation mechanism of Al doped samples, chemical state of Ni at various states of charge is probed by hard XAS (**Figure 5**). The threshold energy position of Ni *K*-edge for all samples is the half-edge energy ($E_{0.5}$) deduced by the half-height method.[71-73] For LANO-05 sample, $E_{0.5}$ value gradually increases with continuous Li^+ extraction from the electrode material towards 4.5 V, and remains almost unchanged until 5.0 V charge. As for LANO-10 and LANO-20 samples, $E_{0.5}$

of Ni *K*-edge reaches the highest value at 4.8 V, and remains steady at 5.0 V for LANO-10, but decreases for LANO-20 sample. The final Ni oxidation state reaches the maximum in LANO-20 sample. During discharge, $E_{0.5}$ of Ni *K*-edge of all samples displays a continuous decrease. The varied Ni valence change at different charged/discharged states for all three samples suggests the contribution of other electrochemical and/or chemical reactions at high voltages.

Chemical state of bulk lattice oxygen is directly characterized using high-efficiency mapping of resonant inelastic X-ray scattering (mRIXS) (**Figure 6**, **7**) for LANO-10 and LANO-20 samples. We did not collect the mRIXS of LANO-05 sample, given its similarities in electrochemistry and phase evolution to $LiNiO_2$.[74] mRIXS is capable of differentiating TM-O hybridization signals from oxygen oxidization state.[52, 53, 74, 75] In particular, a well-defined lattice oxygen oxidation feature emerges at 523.7 eV emission energy and 531.0 eV excitation energy in mRIXS, while broad features around 525 eV emission energy correspond to the TM-O hybridization characters. It is interesting to note that the Ni-O hybridization feature at 528.5 eV excitation energy displays an emission energy splitting when the electrodes are charged up to 4.3 V (white arrow in **Figure 6, 7**), likely due to new RIXS excitations related to Ni oxidation and crystal field changes.[75, 76] More strikingly, the defined oxidized oxygen feature at the excitation and emission energy of 531.0 and 523.7 eV (red arrow), respectively, starts to emerge at 4.5 V during charging, accompanied by the enhancement of low-energy excitations close to the elastic line (dash line) at the same excitation energy.[75] This fingerprinting feature of oxidized oxygen becomes more pronounced upon charging, reaching its maximum intensity at 4.8 V, indicating a continuous oxidation of lattice oxygen during the charging process. During discharge, the feature becomes less visible at 4.0 V discharge and completely disappears when discharged down to 2.7 V. The enhancement of this oxygen oxidation feature during charge and its reversible decrease during discharge clearly suggest the contribution of reversible lattice oxygen redox in the LANO-10 sample. The mRIXS of the LANO-20 system displays essentially a similar reversible evolution of the oxygen redox feature

(red arrow in **Figure 7**). However, the oxidized O feature at high voltages shows a higher intensity in mRIXS, indicating the stronger oxygen redox reactions in LANO-20 compared to LANO-10 sample. Such an observation provides a direct experimental evidence that the lattice oxygen redox reactions are promoted upon inactive Al substitution in LNAO systems, although the oxygen redox feature in these convention layered oxides is much less pronounced compared to that in Li-rich layer oxide reported elsewhere.[52]

3.5. Gas evolution and surface chemical evolution

Apart from studying reversible bulk oxygen redox, we also investigate gas evolution during initial cycle using *operando* differential electrochemical mass spectrometry (DEMS) (**Figure 8**). The onset voltage of oxygen gas release occurs around 4.2 V, which reaches the maximum at 4.65, 4.75 and 4.85 V for LANO-05, LANO-10 and LANO-20, respectively. On the other hand, LANO-05 and LANO-10 yield similar total oxygen gas release (0.025 and 0.023 μmol mg^{-1}, corresponding to 0.24% and 0.22% lattice O, respectively), however, more oxygen release is detected for LANO-20 (0.074 μmol mg^{-1}, 0.68% lattice O). The increased oxygen gas release in LANO-20 is consistent with the stronger oxygen redox signature from mRIXS and more surface Ni reduction from soft XAS at highly charged states (**Figure S6**). If we assume all O in released O_2 gas results from the active material, the released O_2 from LANO-20 would only contribute a capacity of 8 mAh g^{-1}. On the other hand, the onset and maximal voltage of CO_2 evolution are similar for all samples and independent of Al content, which is consistent with its origin from carbonate residual during material synthesis as well as electrolyte oxidation.[65] These results also align with soft XAS O *K*-edge data (**Figure S7**), revealing the presence of carbonate at pristine state until 4.8 V charge for all samples.

3.6. Discussion on the phase transition and oxygen redox

Here, we show that Al doping is effective to suppress the phase transition by promoting Li/Ni intermixing and creating Ni pillars in the Li slabs. More specifically, the H2 to H3 phase transition is

greatly mitigated and delayed to higher voltages with increasing Al content. However, lattice *c* collapse is found to occur upon ~70% Li^+ extraction consistently for all samples, even Ni-rich NCA and NMCs.[68] Combining electrochemistry, structural analysis and mRIXS results, we found a strong correlation between the oxygen oxidation and lattice *c* collapse process in these Ni-based compounds. As summarized in **Figure 9**, the occurrence and disappearance of lattice oxygen redox are coupled with the H2-H3 phase transition (i.e., Li content or *c* collapse). This phenomenon is possible as the *c* collapse in oxygen close-packed layered matrix results in the shortened O-O bonding between interlayers,[70, 77] which is favored for the occurrence of oxygen oxidation. Meanwhile, the gradual increase in the repulsion of O between the TM slabs caused by H2-H3 transition (i.e., *c* collapse) can be accommodated by the loss of electron from lattice O_{2p}^{2-}. However, the degree of the lattice collapse is not necessarily proportional to the participation of oxygen redox in the charge compensation. Instead, the contribution of the oxygen redox is chemistry dependent. With Al doping, less *c* lattice collapse and more oxygen redox are observed. The intensity of oxygen redox in RIXS maps does increase with the Al doping content. This is because with more Al doping content, less cationic Ni redox is accessible, which warrants the available Li^+ to accommodate the oxygen oxidation, therefore, more oxygen redox with increased irreversible O_2 release from the surface upon exposure to the electrolyte. Furthermore, the oxygen gas evolution occurs at the material surface, which is different from the bulk phenomena of oxygen redox and phase evolution. The more oxygen gas release from LANO-20 sample indicates Al doping cannot stabilize the lattice oxygen at the material surface. Therefore, an optimal content and effective surface modification are necessary to stabilize the oxygen and protect it against electrolyte in order to enable long-term cycling of high-capacity Ni-rich layered oxides.

4. Conclusion

In summary, this work unveils multi-faceted roles of Al doping in Ni-based layered oxide cathode. Al doping up to 20 mol% in lithium nickel oxide leads to good layered structure, but facilitates Li/Ni

intermixing to a certain extent. Al doping greatly alleviates the unfavorable phase transition, especially H2-H3 transition. Spectroscopic studies reveal that lattice oxygen redox occurs at high voltages (>4.3 V) and is promoted by inactive Al doping, but excess Al promotes oxygen release and surface Ni reduction. This work illustrates the inevitable *c* lattice collapse due to the H2-H3 phase transition depends on Li content, but not charge voltage, and it is coupled with lattice oxygen redox. Careful evaluation of the optimal range of Al doping under the practical condition is essential to enable high-capacity and long-cycling Ni-rich layered cathode.

Conflicts of Interest

The authors declare no conflicts of interest.

Acknowledgements

Support of this work was provided by the Energy & Biosciences Institute through the EBI-Shell program. We also thank the support from the Assistant Secretary for Energy Efficiency and Renewable Energy, Office of Vehicle Technologies of the U.S. Department of Energy under Contract No. DE-AC02-05CH11231. Use of the Stanford Synchrotron Radiation Lightsource, SLAC National Accelerator Laboratory, is supported by the U.S. Department of Energy, Office of Science, Office of Basic Energy Sciences under Contract No. DE-AC02-76SF00515. This research uses resources of the Advanced Light Source, which is a DOE Office of Science User Facility under contract no. DE-AC02-05CH11231.

References

[1] M. Armand, J.-M. Tarascon, Nature, 451 (2008) 652.
[2] J. B. Goodenough, Y. Kim, J. Power Sources, 196 (2011) 6688-6694.
[3] M. S. Whittingham, Chem. Rev., 104 (2004) 4271-4302.
[4] K. Mizushima, P. Jones, P. Wiseman, J. B. Goodenough, Mater. Res. Bull., 15 (1980) 783-789.
[5] T. Ohzuku, A. Ueda, M. Nagayama, Y. Iwakoshi, H. Komori, Electrochim. Acta, 38 (1993) 1159-1167.
[6] J. Xu, F. Lin, M. M. Doeff, W. Tong, J. Mater. Chem. A, 5 (2017) 874-901.
[7] Y.-K. Sun, S.-T. Myung, B.-C. Park, J. Prakash, I. Belharouak, K. Amine, Nat. Mater., 8 (2009) 320.
[8] Y. K. Sun, Z. Chen, H. J. Noh, D. J. Lee, H. G. Jung, Y. Ren, S. Wang, C. S. Yoon, S. T. Myung, K. Amine, Nat. Mater., 11 (2012) 942-947.
[9] S. T. Myung, H. J. Noh, S. J. Yoon, E. J. Lee, Y. K. Sun, J. Phys. Chem. Lett., 5 (2014) 671-679.
[10] C. Tian, F. Lin, M. M. Doeff, Accounts Chem. Res., 51 (2017) 89-96.

[11] C. S. Yoon, U.-H. Kim, G.-T. Park, S. J. Kim, K.-H. Kim, J. Kim, Y.-K. Sun, ACS Energy Lett., 3 (2018) 1634-1639.
[12] H.-H. Ryu, G.-T. Park, C. S. Yoon, Y.-K. Sun, J. Mater. Chem. A, 7 (2019) 18580-18588.
[13] R. Robert, C. Bünzli, E. J. Berg, P. Novák, Chem. Mater., 27 (2015) 526-536.
[14] A. Grenier, H. Liu, K. M. Wiaderek, Z. W. Lebens-Higgins, O. J. Borkiewicz, L. F. J. Piper, P. J. Chupas, K. W. Chapman, Chem. Mater., 29 (2017) 7345-7352.
[15] K. Märker, P. J. Reeves, C. Xu, K. J. Griffith, C. P. Grey, Chem. Mater., 31 (2019) 2545-2554.
[16] H. Li, N. Zhang, J. Li, J. R. Dahn, J. Electrochem. Soc., 165 (2018) A2985-A2993.
[17] T. Ohzuku, A. Ueda, M. Nagayama, J. Electrochem. Soc., 140 (1993) 1862-1870.
[18] H. S. Liu, Z. R. Zhang, Z. L. Gong, Y. Yang, Electrochem. Solid-State Lett., 7 (2004) A190.
[19] A. Rougier, P. Gravereau, C. Delmas, J. Electrochem. Soc., 143 (1996) 1168-1175.
[20] H. Das, A. Urban, W. Huang, G. Ceder, Chem. Mater., 29 (2017) 7840-7851.
[21] P. Kalyani, N. Kalaiselvi, Sci. Technol. Adv. Mat., 6 (2016) 689-703.
[22] C. S. Yoon, D.-W. Jun, S.-T. Myung, Y.-K. Sun, ACS Energy Lett., 2 (2017) 1150-1155.
[23] J. Xu, E. Hu, D. Nordlund, A. Mehta, S. N. Ehrlich, X.-Q. Yang, W. Tong, ACS Appl. Mater. Interfaces, 8 (2016) 31677-31683.
[24] M. Guilmard, L. Croguennec, C. Delmas, Chem. Mater., 15 (2003) 4484-4493.
[25] M. Guilmard, L. Croguennec, D. Denux, C. Delmas, Chem. Mater., 15 (2003) 4476-4483.
[26] K. Ishidzu, Y. Oka, T. Nakamura, Solid State Ionics, 288 (2016) 176-179.
[27] H.-H. Ryu, K.-J. Park, C. S. Yoon, Y.-K. Sun, Chem. Mater., 30 (2018) 1155-1163.
[28] J. Li, R. Shunmugasundaram, R. Doig, J. Dahn, Chem. Mater., 28 (2015) 162-171.
[29] M. A. Cambaz, B. P. Vinayan, H. Geßwein, A. Schiele, A. Sarapulova, T. Diemant, A. Mazilkin, T. Brezesinski, R. J. Behm, H. Ehrenberg, Chem. Mater., 31 (2019) 4330-4340
[30] C. S. Yoon, H.-H. Ryu, G.-T. Park, J.-H. Kim, K.-H. Kim, Y.-K. Sun, J. Mater. Chem. A, 6 (2018) 4126-4132.
[31] U.-H. Kim, J.-H. Kim, J.-Y. Hwang, H.-H. Ryu, C. S. Yoon, Y.-K. Sun, Mater. Today, 23 (2019) 26-36.
[32] J.-H. Kim, K.-J. Park, S. J. Kim, C. S. Yoon, Y.-K. Sun, J. Mater. Chem. A, 7 (2019) 2694-2701.
[33] J.-H. Kim, H.-H. Ryu, S.J. Kim, C. S. Yoon, Y.-K. Sun, ACS Appl. Mater. Interfaces, 11 (2019) 30936-30942.
[34] K.-J. Park, J.-Y. Hwang, H.-H. Ryu, F. Maglia, S.-J. Kim, P. Lamp, C. S. Yoon, Y.-K. Sun, ACS Energy Lett., 4 (2019) 1394-1400.
[35] F. Schipper, E. M. Erickson, C. Erk, J.-Y. Shin, F. F. Chesneau, D. Aurbach, J. Electrochem. Soc., 164 (2017) A6220-A6228.
[36] S.-T. Myung, F. Maglia, K.-J. Park, C. S. Yoon, P. Lamp, S.-J. Kim, Y.-K. Sun, ACS Energy Lett., 2 (2016) 196-223.
[37] A. Manthiram, J. C. Knight, S.-T. Myung, S.-M. Oh, Y.-K. Sun, Adv. Energy Mater., 6 (2016) 1501010.
[38] Q. Xie, W. Li, A. Manthiram, Chem. Mater., 31 (2019) 938-946.
[39] L. Zou, J. Li, Z. Liu, G. Wang, A. Manthiram, C. Wang, Nat. Commun., 10 (2019) 3447.
[40] N. V. Faenza, N. Pereira, D. M. Halat, J. Vinckeviciute, L. Bruce, M. D. Radin, P. Mukherjee, F. Badway, A. Halajko, F. Cosandey, Chem. Mater., 30 (2018) 7545-7574.
[41] Z. Lu, J. R. Dahn, J. Electrochem. Soc., 149 (2002) A815.
[42] A. R. Armstrong, M. Holzapfel, P. Novák, C. S. Johnson, S.-H. Kang, M. M. Thackeray, P. G. Bruce, J. Am. Chem. Soc., 128 (2006) 8694-8698.
[43] M. M. Thackeray, S.-H. Kang, C. S. Johnson, J. T. Vaughey, R. Benedek, S. Hackney, J. Mater. Chem., 17 (2007) 3112-3125.

[44] N. Tran, L. Croguennec, M. Ménétrier, F. Weill, P. Biensan, C. Jordy, C. Delmas, Chem. Mater., 20 (2008) 4815-4825.
[45] Z. W. Lebens-Higgins, N. V. Faenza, M. D. Radin, H. Liu, S. Sallis, J. Rana, J. Vinckeviciute, P. J. Reeves, M. J. Zuba, F. Badway, N. Pereira, K. W. Chapman, T.-L. Lee, T. Wu, C. P. Grey, B. C. Melot, A. Van Der Ven, G. G. Amatucci, W. Yang, L. F. J. Piper, Mater. Horiz., 6 (2019) 2112-2123.
[46] H. Koga, L. Croguennec, M. Ménétrier, P. Mannessiez, F. Weill, C. Delmas, J. Power Sources, 236 (2013) 250-258.
[47] H. Koga, L. Croguennec, M. Ménétrier, P. Mannessiez, F. Weill, C. Delmas, S. Belin, J. Phys. Chem. C, 118 (2014) 5700-5709.
[48] H. Koga, L. Croguennec, M. Ménétrier, K. Douhil, S. Belin, L. Bourgeois, E. Suard, F. Weill, C. Delmas, J. Electrochem. Soc., 160 (2013) A786-A792.
[49] K. Luo, M. R. Roberts, R. Hao, N. Guerrini, D. M. Pickup, Y. S. Liu, K. Edstrom, J. Guo, A. V. Chadwick, L. C. Duda, P. G. Bruce, Nat. Chem., 8 (2016) 684-691.
[50] M. Sathiya, G. Rousse, K. Ramesha, C. P. Laisa, H. Vezin, M. T. Sougrati, M. L. Doublet, D. Foix, D. Gonbeau, W. Walker, A. S. Prakash, M. Ben Hassine, L. Dupont, J. M. Tarascon, Nat. Mater., 12 (2013) 827-835.
[51] D. H. Seo, J. Lee, A. Urban, R. Malik, S. Kang, G. Ceder, Nat. Chem., 8 (2016) 692-697.
[52] J. Xu, M. Sun, R. Qiao, S. E. Renfrew, L. Ma, T. Wu, S. Hwang, D. Nordlund, D. Su, K. Amine, J. Lu, B. D. McCloskey, W. Yang, W. Tong, Nat. Commun., 9 (2018) 947.
[53] W. E. Gent, K. Lim, Y. Liang, Q. Li, T. Barnes, S.-J. Ahn, K. H. Stone, M. McIntire, J. Hong, J. H. Song, Nat. Commun., 8 (2017) 2091.
[54] R. Jung, M. Metzger, F. Maglia, C. Stinner, H. A. Gasteiger, J. Electrochem. Soc., 164 (2017) A1361-A1377.
[55] A. Gupta, W. D. Chemelewski, C. Buddie Mullins, J. B. Goodenough, Adv. Mater., 27 (2015) 6063-6067.
[56] S.-M. Bak, K.-W. Nam, W. Chang, X. Yu, E. Hu, S. Hwang, E. A. Stach, K.-B. Kim, K. Y. Chung, X.-Q. Yang, Chem. Mater., 25 (2013) 337-351.
[57] K.-W. Nam, S.-M. Bak, E. Hu, X. Yu, Y. Zhou, X. Wang, L. Wu, Y. Zhu, K.-Y. Chung, X.-Q. Yang, Adv. Funct. Mater., 23 (2013) 1047-1063.
[58] W.-S. Yoon, K.-B. Kim, M.-G. Kim, M.-K. Lee, H.-J. Shin, J.-M. Lee, J.-S. Lee, C.-H. Yo, J. Phys. Chem. B, 106 (2002) 2526-2532.
[59] L. de Biasi, A. Schiele, M. Roca-Ayats, G. Garcia, T. Brezesinski, P. Hartmann, J. Janek, ChemSusChem, 12 (2019) 2240-2250.
[60] G. Amatucci, J. Tarascon, L. Klein, J. Electrochem. Soc., 143 (1996) 1114-1123.
[61] M. Aydinol, A. Kohan, G. Ceder, K. Cho, J. Joannopoulos, Phys. Rev. B, 56 (1997) 1354.
[62] G. Ceder, Y.-M. Chiang, D. Sadoway, M. Aydinol, Y.-I. Jang, B. Huang, Nature, 392 (1998) 694.
[63] J.-N. Zhang, Q. Li, C. Ouyang, X. Yu, M. Ge, X. Huang, E. Hu, C. Ma, S. Li, R. Xiao, Nat. Energy, (2019) 1.
[64] M. Jo, M. Noh, P. Oh, Y. Kim, J. Cho, Adv. Energy Mater., 4 (2014) 1301583.
[65] S. E. Renfrew, B. D. McCloskey, J. Am. Chem. Soc., 139 (2017) 17853-17860.
[66] J. Li, N. Zhang, H. Li, A. Liu, Y. Wang, S. Yin, H. Wu, J. R. Dahn, J. Electrochem. Soc., 165 (2018) A3544-A3557.
[67] T. Ohzuku, A. Ueda, M. Kouguchi, J. Electrochem. Soc., 142 (1995) 4033-4039.
[68] H. Li, A. Liu, N. Zhang, Y. Wang, S. Yin, H. Wu, J. R. Dahn, Chem. Mater., 31 (2019) 7574-7583.
[69] J. Xu, S. Renfrew, M. A. Marcus, M. Sun, B. D. McCloskey, W. Tong, J. Phys. Chem. C, 121 (2017) 11100-11107.
[70] G. Assat, J.-M. Tarascon, Nat. Energy, (2018) 1.
[71] H. Dau, P. Liebisch, M. Haumann, Anal. Bioanal. Chem., 376 (2003) 562-583.

[72] X. Yu, Y. Lyu, L. Gu, H. Wu, S.-M. Bak, Y. Zhou, K. Amine, S. N. Ehrlich, H. Li, K.-W. Nam, X.-Q. Yang, Adv. Energy Mater., 4 (2014) 1300950.
[73] Q.-C. Wang, J.-K. Meng, X.-Y. Yue, Q.-Q. Qiu, Y. Song, X.-J. Wu, Z.-W. Fu, Y.-Y. Xia, Z. Shadike, J. Wu, J. Am. Chem. Soc., 141 (2018) 840-848.
[74] N. Li, S. Sallis, J. K. Papp, J. Wei, B. D. McCloskey, W. Yang, W. Tong, ACS Energy Lett., (2019) 2836-2842.
[75] J. Wu, Q. Li, S. Sallis, Z. Zhuo, W. Gent, W. Chueh, S. Yan, Y.-D. Chuang, W. Yang, Condens. Matter, 4 (2019) 5.
[76] W. Yang, T. P. Devereaux, J. Power Sources, 389 (2018) 188-197.
[77] M. Saubanère, E. McCalla, J. M. Tarascon, M. L. Doublet, Energy Environ. Sci., 9 (2016) 984-991.

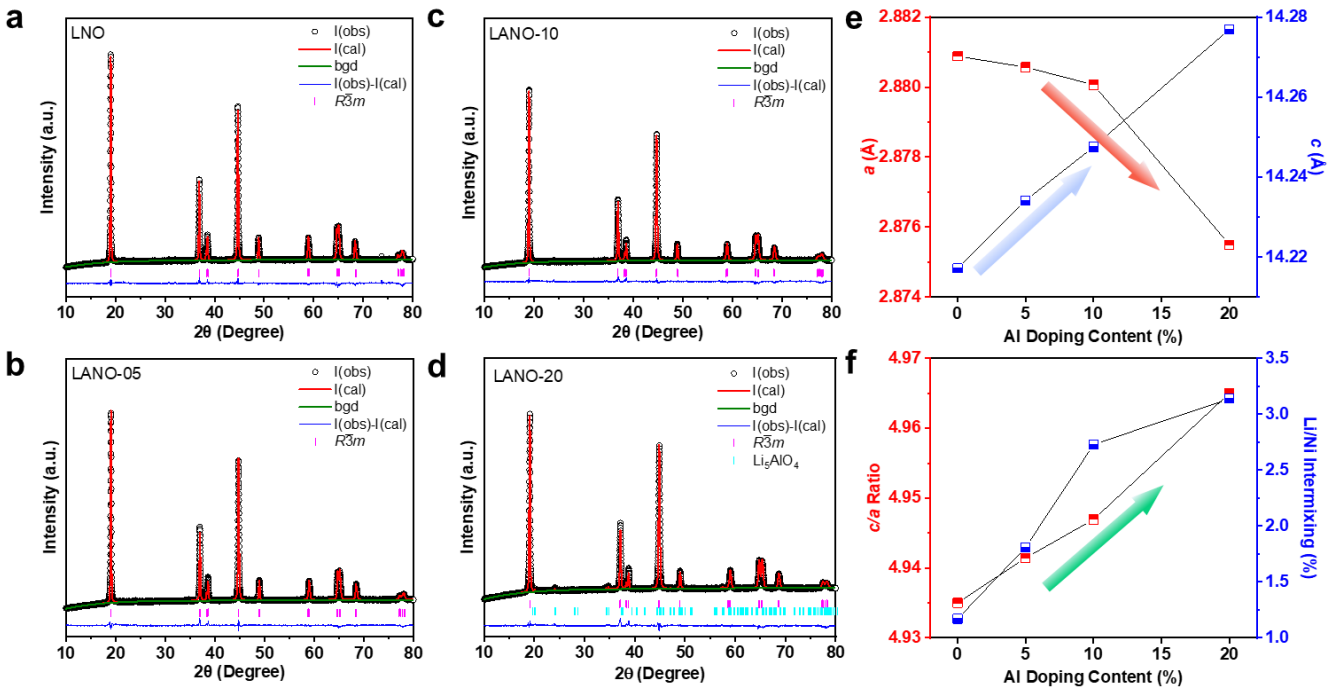

Figure 1. Structural characterization of all samples along with Rietveld fits. (a) LNO, (b) LANO-05, (c) LANO-10, (d) LANO-20, (e) lattice parameter *a* and *c*, and (f) *c*/*a* ratio and Li/Ni intermixing as a function of Al content.

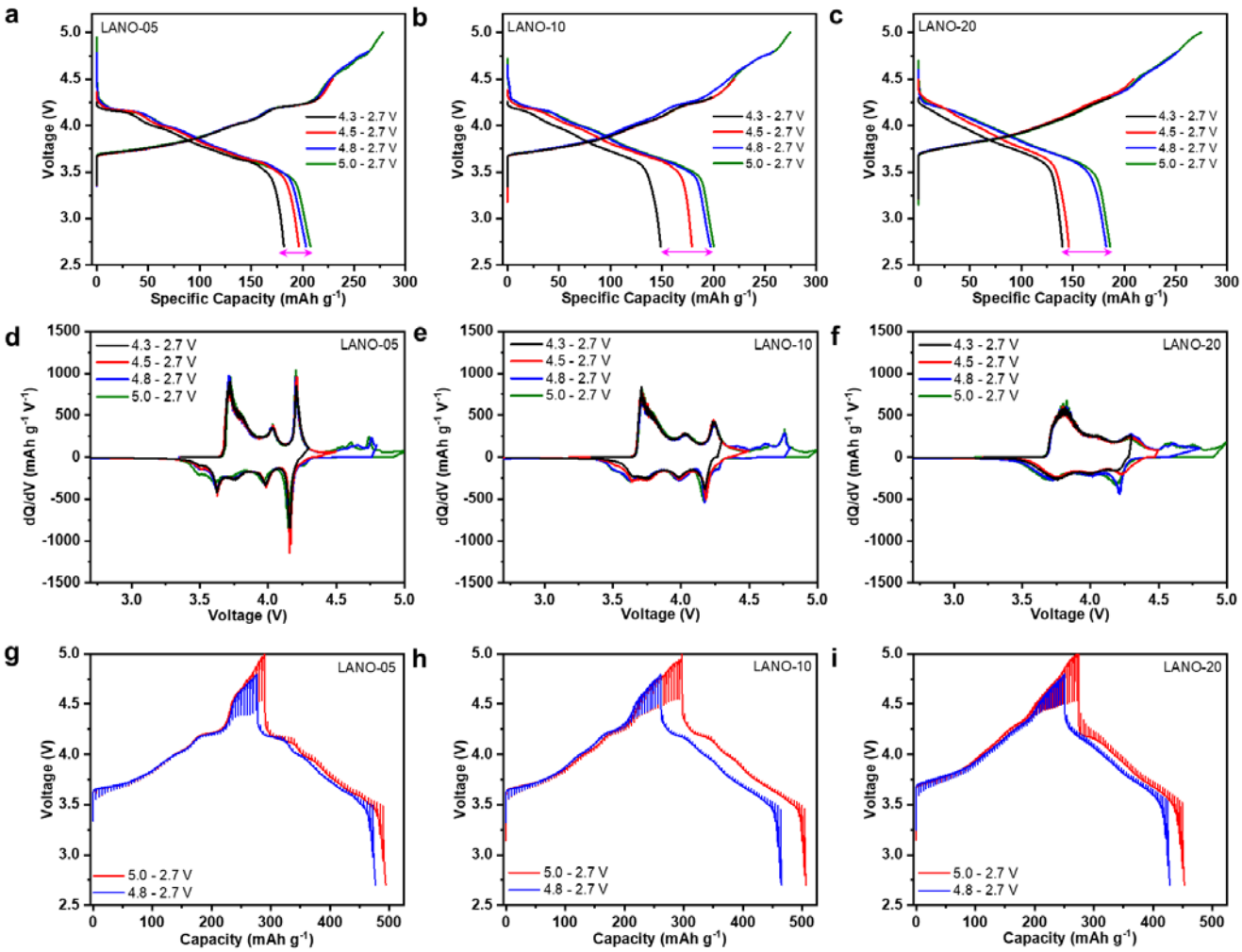

Figure 2. Electrochemical performance of LANO samples at different charge cutoff voltages. (a-c) The first charge-discharge voltage profiles, (d-f) the first-cycle dQ/dV plots at 20 mA g^{-1} and (g-i) GITT profiles at charge cutoff voltages of 4.8 and 5.0 V. All samples for GITT tests are charged at 10 mA g^{-1} for 0.5 h and rest for 3 h.

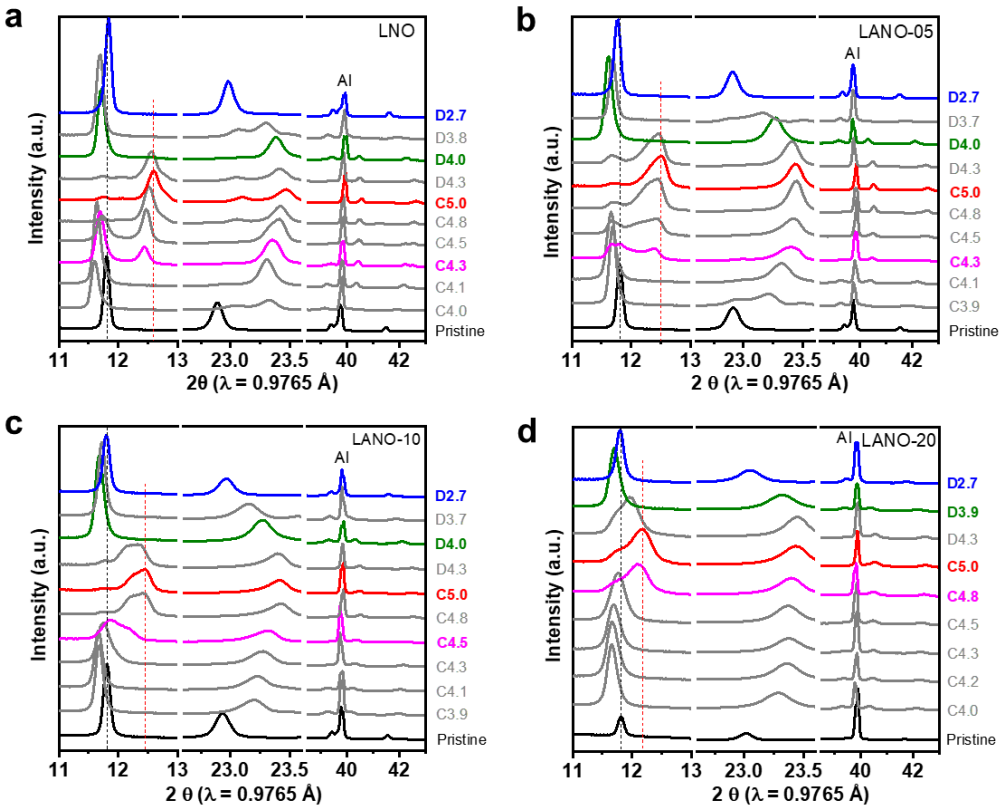

Figure 3. Phase evolution of all samples during charge and discharge determined by *ex situ* wide angle X-ray scattering (WAXS). (a) LNO, (b) LANO-05, (c) LANO-10 and (d) LANO-20. X-ray beam is set at a fixed energy of 12.7 KeV and wavelength of 0.9765 Å.

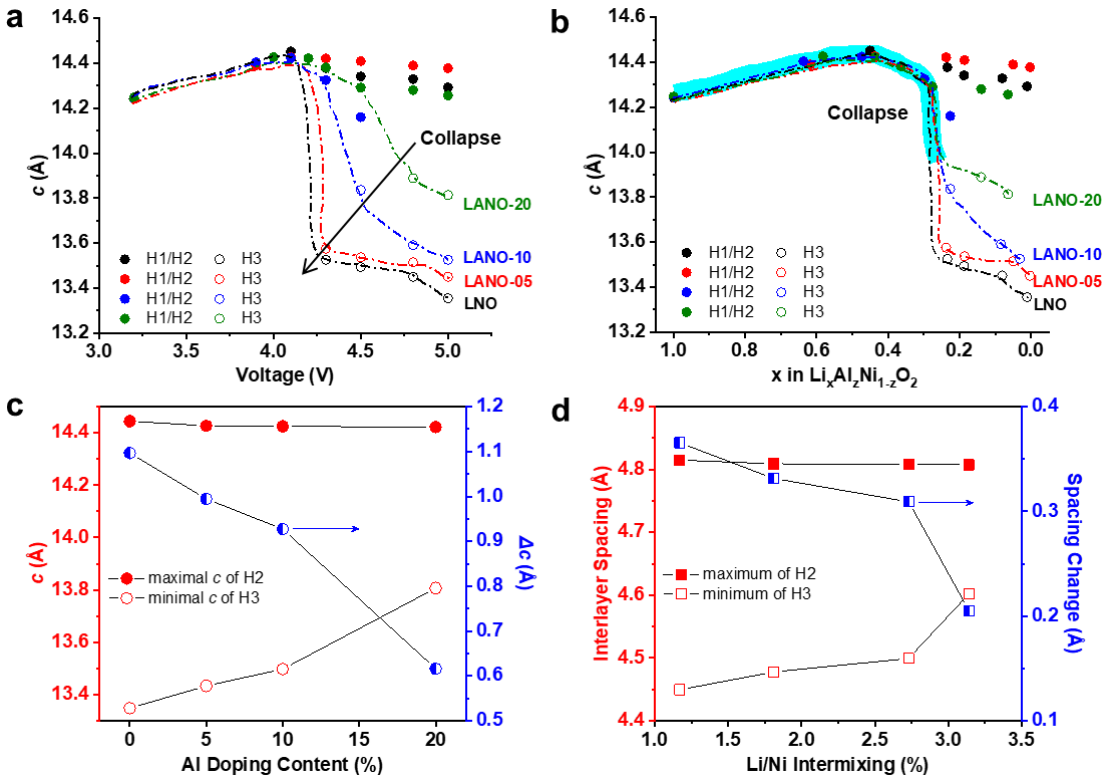

Figure 4. Lattice parameters calculated from *ex situ* WAXS for all samples during charge and discharge. Lattice *c* as a function of (a) voltage and (b) Li content in the electrode, (c) lattice *c* of H2 and H3 phase along with its variation as a function of Al doping content and (d) interlayer spacing of H2 and H3 phase along with its variation as a function of Li/Ni intermixing.

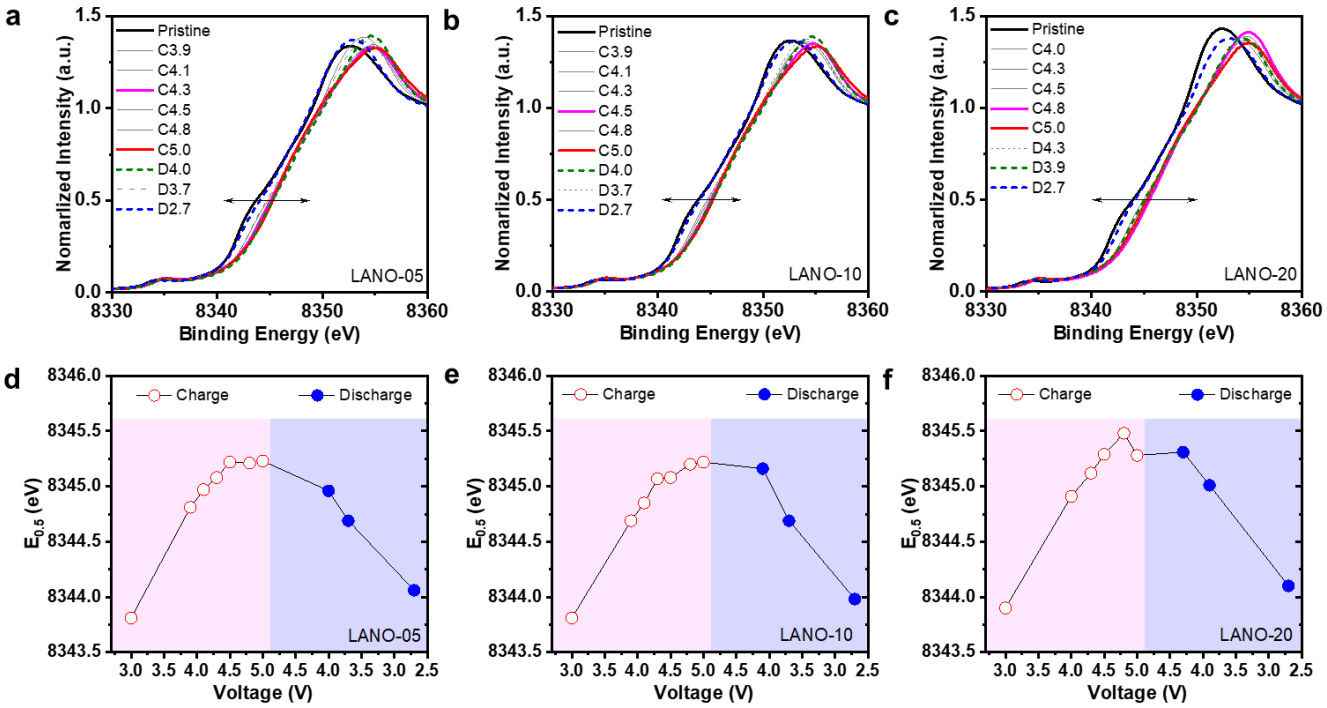

Figure 5. Chemical state of bulk Ni at various states of charge for all Al-doped samples. (a, b, c) Ni *K*-edge XANES and (d, e, f) the corresponding half-edge energy ($E_{0.5}$) for LANO-05, LANO-10 and LANO-20, respectively.

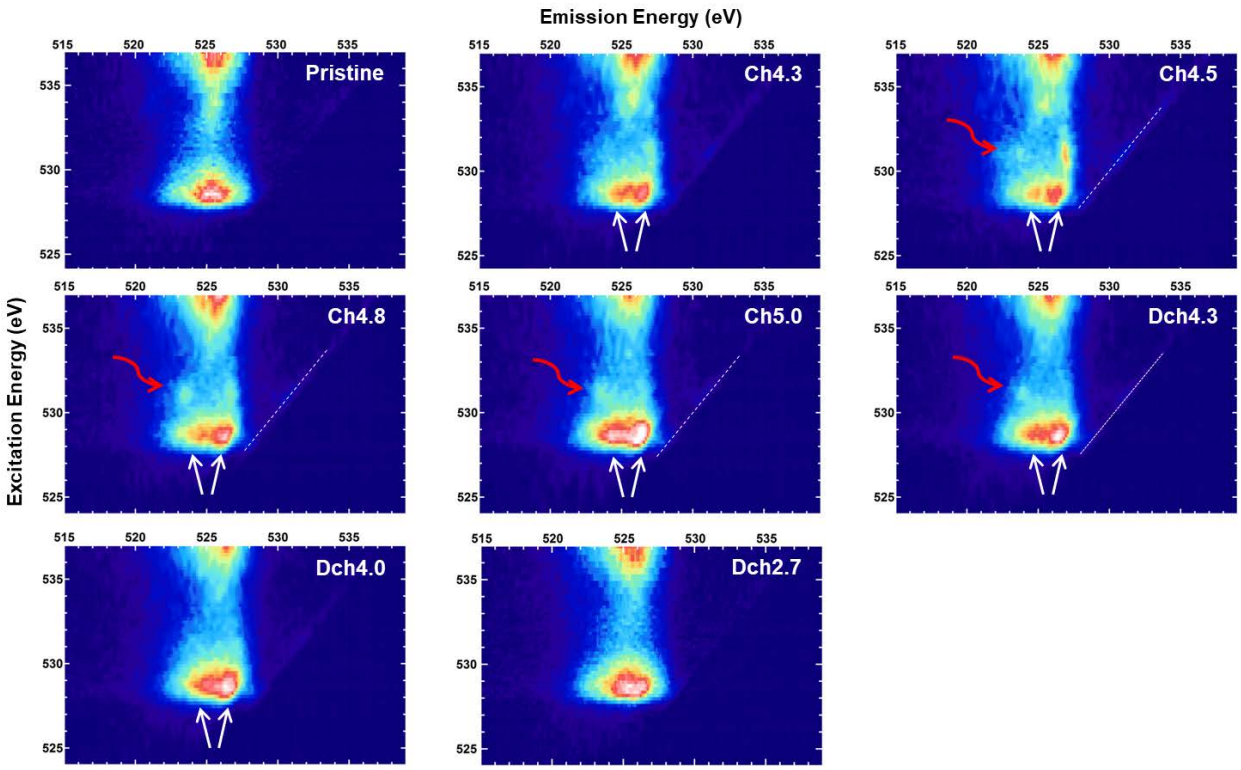

Figure 6. Chemical state of O in LANO-10 probed by RIXS O *K*-edge mapping at different states of charge.

Red, white arrow and dash line mark lattice oxygen redox, TM-O hybridization and elastic feature, respectively.

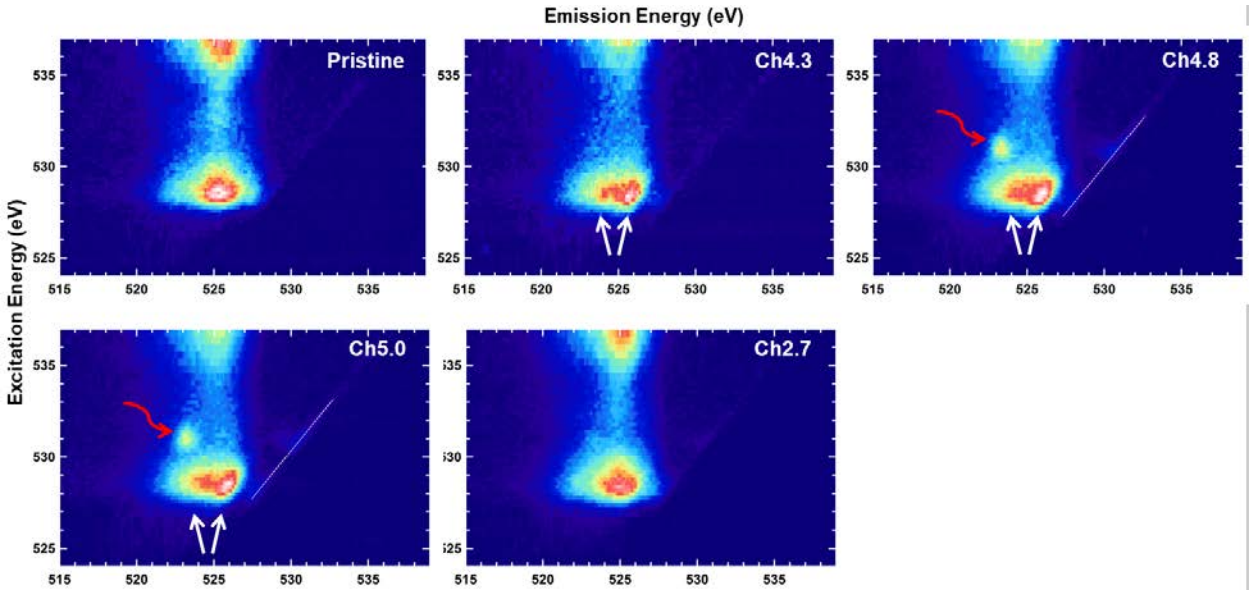

Figure 7. Chemical state of O in LANO-20 probed by RIXS O *K*-edge mapping at different states of charge.

Red, white arrow and dash line mark lattice oxygen redox, TM-O hybridization and elastic feature, respectively.

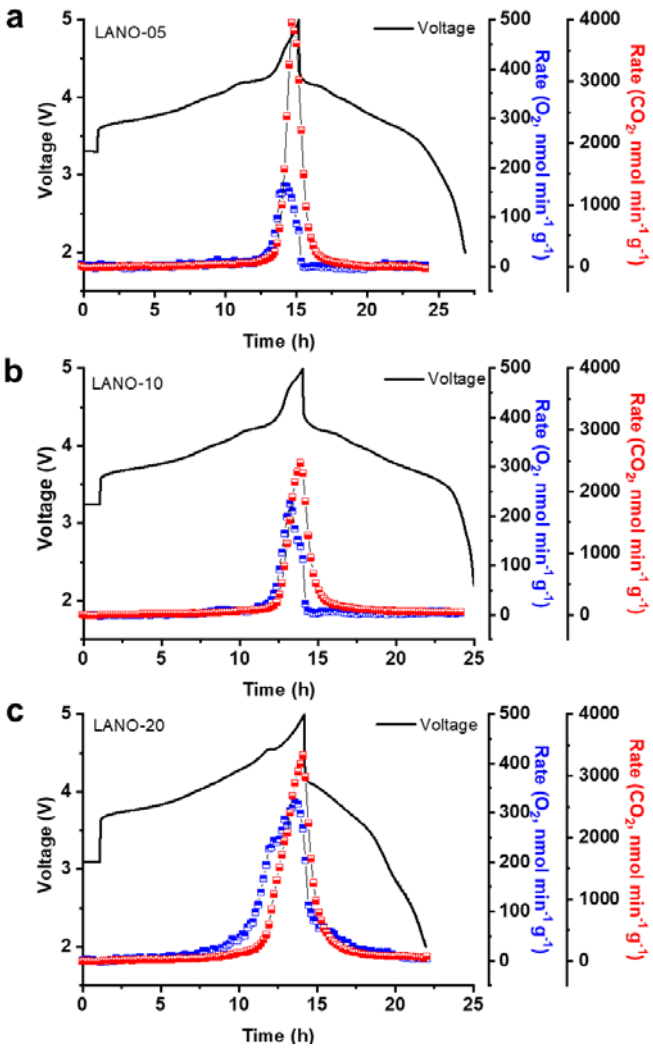

Figure 8. Gas evolution during the first cycle of Al-doped samples determined by *operando* DEMS. (a) LANO-05, (b) LANO-10 and (c) LANO-20. Cells are cycled between 5.0 and 2.7 V at 20 mA g^{-1}.

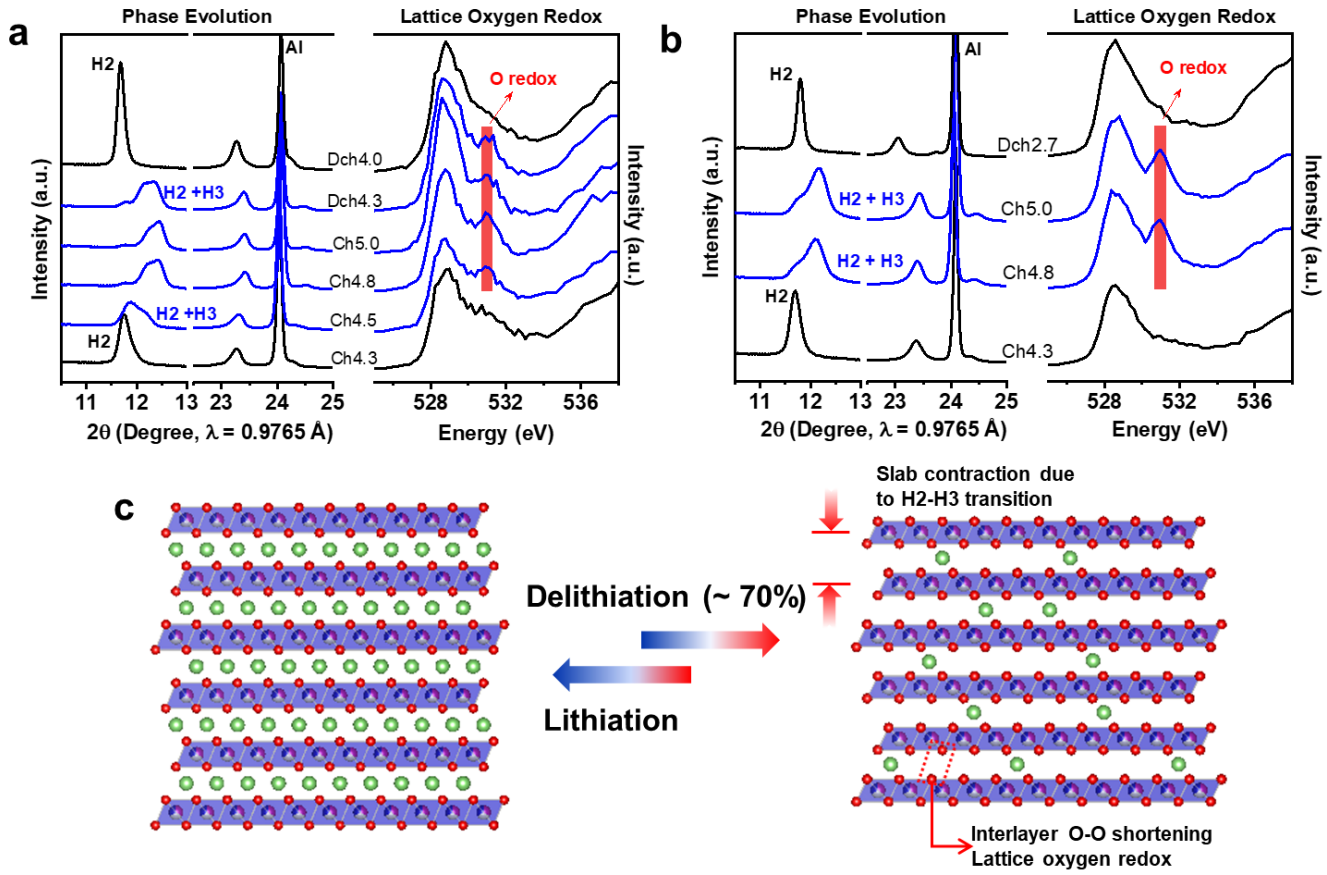

Figure 9. Occurrence of phase evolution and lattice oxygen redox in layered cathodes. *Ex situ* WAXS patterns (left) and sPFY obtained from O *K*-edge RIXS maps (right) at different states of charge for (a) LANO-10 and (a) LANO-20 samples, and (b) schematic diagram showing the phase evolution and lattice oxygen redox upon (de)lithiation of layered cathodes.

Dr. Ning Li is currently an associate Professor in the School of Materials Science and Engineering at Beijing Institute of Technology (BIT). He worked as a postdoctoral fellow at Lawrence Berkeley National Laboratory from 2016 to 2020. He received his B.S. in Environmental Engineering in 2009 and Ph.D. in Applied Chemistry in 2015 at Beijing Institute of Technology, China. His research focuses on the design and synthesis of high-performance electrode materials, especially oxygen redox related cathodes, for Li-ion and Na-ion batteries, silicon-based anodes, and synchrotron-based material diagnostics.

Dr. Shawn Sallis received his PhD in Materials Science from Binghamton University in 2017. He worked with Wanli Yang as a Postdoctoral fellow at the Advanced Light Source for 2 years before moving on to a position in industry. His scientific interests lie in X-ray metrology with a focus on spectroscopy of oxides and novel semiconductors for functional materials and applying machine learning to the analysis of scientific data.

Joseph K. Papp received his B.S. degree in Chemical Engineering from the University of Kentucky in 2015. He is currently a Ph.D. candidate in the Department of Chemical & Biomolecular Engineering at UC Berkeley. His research interests are focused on high voltage instabilities for Li-ion battery cathodes.

Dr. Bryan McCloskey is an Associate Professor and the Vice Chair of Graduate Education in the Department of Chemical and Biomolecular Engineering at the University of California, Berkeley, and also holds a joint appointment as a Faculty Engineer in the Energy Storage and Distributed Resources Division at Lawrence Berkeley National Laboratory. His laboratory currently focuses on metal-air batteries, photoelectrochemical CO_2 reduction, and a variety of challenges facing Li-ion batteries, including high voltage cathode stability, advanced cathode material development, extreme fast charging, and low temperature and high transference number electrolyte formulations. More information about the McCloskey Lab can be found at the Lab's website: www.mccloskeylab.com.

Dr. Wanli Yang is a senior staff scientist at the Advanced Light Source of Lawrence Berkeley National Laboratory. His research interest focuses on technical developments and scientific applications of soft x-ray spectroscopy for energy sciences. He developed and formalized the quantitative analysis of 3d transition-metal oxidation states on surface and in bulk of battery electrodes through combined spectroscopic tools and fittings. He led the efforts on developing high-efficiency mapping of resonant inelastic x-ray scattering (mRIXS) for battery material research, and introduced mRIXS to the battery field as a tool-of-choice for characterizing the lattice oxygen redox reactions.

Dr. Wei Tong is a Scientist/Principal Investigator in Energy Storage and Distributed Resources Division at Lawrence Berkeley National Laboratory. She obtained her B.S. and M.S. degree in Materials Science at Wuhan University of Technology, China and Ph.D. degree in Materials Science and Engineering at Rutgers University in 2010. Her current research interests focus on the design and synthesis of high-performance electrode materials for Li-ion and beyond Li-ion batteries as well as in-depth understanding of the reaction mechanism through combined electrochemical analysis and advanced characterizations.